Ablation of sloping ice faces into polar sea water

Mainak Mondal[1]†, Bishakhdatta Gayen[1]‡ Ross W. Griffiths[1] and Ross C. Kerr,[1]

[1]Research School of Earth Sciences, The Australian National University, ACT, Australia

(Received xx; revised xx; accepted xx)

The effects of the slope of an ice-seawater interface on the mechanisms and rate of ablation of the ice by natural convection are examined using turbulence resolving simulations. Solutions are obtained for ice slopes $\theta = 2^{\circ} - 90^{\circ}$, at a fixed ambient salinity and temperature, chosen to represent common Antarctic ocean conditions. For laminar boundary layers the ablation rate decreases with height, whereas in the turbulent regime, the ablation rate is found to be height independent. The simulated laminar ablation rates scale with $(\sin\theta)^{1/4}$, whereas in the turbulent regime it follows a $(\sin\theta)^{2/3}$ scaling, both consistent with theoretical predictions developed here. The reduction in the ablation rate with shallower slopes arises as a result of the development of stable density stratification beneath the ice face which reduces turbulent buoyancy fluxes to the ice. The turbulent kinetic energy budget of the flow shows that for very steep slopes both buoyancy and shear production are drivers of turbulence, whereas for shallower slopes shear production becomes the dominant mechanism for sustaining turbulence in the convective boundary layer.

1. Introduction

The loss of Antarctic ice shelves is contributing to global ocean sea level rise as a result of volumetric in-flux (Cazenave & Llovel 2010; Piecuch & Ponte 2014). Glacier melting is also contributing to a stronger fresh water layer over the Weddell Sea, which can reduce the formation of Antarctic Bottom Water, an important component in the global thermohaline circulation (Lavergne *et al.* 2014). Recent studies report that the rate of loss of the grounded ice mass of West Antarctica has increased by 70% since 2002 (Paolo *et al.* 2016). Much of this acceleration has been attributed to the intrusion of warmer circumpolar deep water under ice shelf cavities (Jenkins *et al.* 2010; Jacobs *et al.* 2011). However the underlying dynamics of ice melting is quite complex and poorly understood, involving the transport of heat and salt through a thin boundary layer at the ice face. Numerical studies with General Circulation Models (GCMs) (Swingedouw *et al.* 2008; Beckmann & Goosse 2003; Spence *et al.* 2014; Snow *et al.* 2016) and regional ocean models (Galton-Fenzi *et al.* 2012) have modelled the melting and the Antarctic ice cover. Numerical modelling of the dynamics of Pine Island Glacier and it's grounding line has shown a tight coupling between the ice sheet interior and the surrounding ocean properties (Rydt & Gudmundsson 2016). Such models resolve the flow-field at scales larger than $>$O(100) m and rely on parameterisations for the convection and turbulent processes controlling the melt rate. These parameterisations are also not coupled to the grid resolution, thereby exacerbating the uncertainty in the resulting model solutions

† Email address for correspondence: mainak.mondal@anu.edu.au
‡ Email address for correspondence: bishakhdatta.gayen@anu.edu.au

(Morrison *et al.* 2011; Gladish *et al.* 2012). Turbulence-resolving simulations are helpful in understanding the mechanisms governing the melting process. This will improve the parameterisations for larger scale models, enabling them to predict melt rates more accurately.

Laboratory experiments with a small ice block, immersed in warm water with a vertical salinity gradient, showed a laminar boundary layer next to the ice face and the formation of double diffusive horizontal intrusions (Huppert & Turner 1978, 1980; Carey & Gebhart 1982). Experiments on the ablation of a relatively tall (O(1 m)) and vertical ice surface in colder and saline (35 ‰) water of uniform far-field conditions (Josberger & Martin 1981) achieved a turbulent boundary layer. A recent experimental study (Kerr & McConnochie 2015) revisited the turbulent ablation of a vertical wall with ambient water temperatures ($0-6$ °C) and salinity (35 ‰) close to those of Antarctic waters and showed that the melt rate is independent of height. The results also imply that natural convection is driven by the salinity buoyancy. Diffusion of salt to the ice interface lowers the melting temperature, allowing the ice to melt (or dissolve) even when the interface temperature is less than 0 °C (Woods 1992; Kerr 1994; Wells & Worster 2011; Kerr & McConnochie 2015).

Scaling laws for the boundary layer properties and ablation rate have been proposed for various flow scenarios. For a laminar boundary layer next to a vertical ice interface a balance between vertical advection by mean flow and lateral diffusion of solute leads to an ablation velocity that scales to the $-1/4$ power of the height, and the $1/4$ power of buoyancy anomaly, the later mostly provided by the salinity field (Josberger & Martin 1981; Carey & Gebhart 1982; Nilson 1985; Wells & Worster 2011). For turbulent boundary layer, on the other hand, a turbulent parameterisation (such as the use of a constant turbulent diffusivity; Josberger & Martin 1981) is necessary. A recent theoretical model for dissolution (based on an established scaling for turbulent heat transfer for natural convection, Holman 2010), predicts that the ablation velocity scales as $V \sim \Delta T_L^{4/3}$, where $\Delta T_L = T_w - T_L$ is the difference between the ambient temperature T_w and the freezing point at ambient salinity T_L (Kerr & McConnochie 2015). The thermal driving $\Delta T_L = T_w - T_L$, and therefore the ablation rate, is controlled by the transport of solute to the ice interface. Kerr & McConnochie (2015) also show that this recently developed theoretical model is consistent with earlier estimation of ice-berg melt rate from ocean measurements (Morgan & Budd 1978; Budd *et al.* 1980; Shepherd *et al.* 2004) and with their own laboratory experiments.

In some of the large scale ocean models the contribution of convection-driven melting at the ice-ocean interface is included through a buoyant plume model and parameterised turbulent fluxes (Payne *et al.* 2007; Jenkins 1991, 2011). The plume model uses the conservation of momentum and heat (Morton *et al.* 1956; Ellison & Turner 1959) for a one-dimensional convective plume with 'top hat' profiles across the plume. The theory is further developed by incorporating the flux equation for salt transport through a solutal boundary layer under a sloping ice interface (Jenkins 2011; Magorrian & Wells 2016; Slater *et al.* 2016). However in these models the boundary layer turbulence is assumed to be driven by shear instability.

Three-dimensional direct numerical simulations (DNS) of the dissolution of ice into saline water, for the case of planar vertical interface (Gayen *et al.* 2016), have showed the dissolution rates in close agreement with the experiments by Josberger & Martin (1981) and Kerr & McConnochie (2015) and with the predicted $4/3$ power dependence on the thermal forcing. The DNS also showed the presence of a logarithmic layer in both

the velocity and density field in the boundary layer. In these models the boundary layer turbulence is assumed to be driven by convective instability.

Observations of glacier tongues on the seaward side the grounding line indicate that the ice-water interface has a wide range of slopes (Jenkins *et al.* 2010). It is melting near the grounding line (Rignot & Jacobs 2002) that is most likely to influence the overall loss of grounded ice and the resulting see level rise through effects on the glacier dynamics. Under a sloping ice face the flow and melting are expected to be complicated by a component of the buoyancy force orthogonal to the sloping face. A potentially stable salinity stratification can develop there. Attempts to describe the melting of a sloping ice boundary (Jenkins 2011; Magorrian & Wells 2016) have used the turbulent buoyant plume theory. However, there are no turbulence resolving simulations to test the scaling for boundary layer properties and melting rate. The energy pathways for production of turbulence, an important consideration for the formulation of parameterisation, are also unknown. Here we investigate the effects of slope on the ablation rate and boundary layer properties for ice in contact with uniform and quiescent surrounding sea water using Direct Numerical Simulation. The simulations show complex boundary layer structures and are used to establish a new scaling theory. The energy pathways to turbulence are also examined.

2. Formulation of the problem and solution techniques

The flow field is solved in a rectangular domain shown in figure 1 with length L parallel to the slope, depth W normal to the ice face and a width D in the spanwise direction (normal to the plane of the schematic). Ice-water interface conditions are applied at one boundary (the ice face) of the computational domain (figure 1). The domain and coordinate system are rotated relative to gravity in order to represent the ice slope. Gravity is always directed downward. The flow field is represented by $\tilde{\mathbf{u}} = [u_\eta,\ v,\ u_\zeta]$, where the wall-normal (η), spanwise (y) and slope-parallel (ζ) directions are u_η, v and u_ζ, respectively. The co-ordinates and velocities are relative to a reference frame fixed at the planar ice water interface. This is the most convenient reference frame and we make no assumption about the relative speeds of the glacier advance and ablation. We solve the incompressible continuity, Navier-Stokes, heat and salt equations:

$$\nabla \cdot \tilde{\mathbf{u}} = 0 \tag{2.1}$$

$$\frac{\partial u_\eta}{\partial t} + (\tilde{\mathbf{u}} \cdot \nabla) u_\eta = -\frac{1}{\rho_0}\frac{\partial p^*}{\partial \eta} + \nu \nabla^2 u_\eta + \frac{\rho^*}{\rho_0} g \cos\theta \tag{2.2}$$

$$\frac{\partial u_\zeta}{\partial t} + (\tilde{\mathbf{u}} \cdot \nabla) u_\zeta = -\frac{1}{\rho_0}\frac{\partial p^*}{\partial \zeta} + \nu \nabla^2 u_\zeta - \frac{\rho^*}{\rho_0} g \sin\theta \tag{2.3}$$

$$\frac{\partial v}{\partial t} + (\tilde{\mathbf{u}} \cdot \nabla) v = -\frac{1}{\rho_0}\frac{\partial p^*}{\partial y} + \nu \nabla^2 v \tag{2.4}$$

$$\frac{\partial T^*}{\partial t} + (\tilde{\mathbf{u}} \cdot \nabla) T^* = \kappa_T \nabla^2 T^* \tag{2.5}$$

$$\frac{\partial S^*}{\partial t} + (\tilde{\mathbf{u}} \cdot \nabla) S^* = \kappa_S \nabla^2 S^* .' \tag{2.6}$$

Here ρ_0 is the reference density for pure water at 0°C and p^*, T^*, S^* and ρ^* denote the deviation from the ambient hydrostatic pressure (p_w), temperature (T_w), salinity

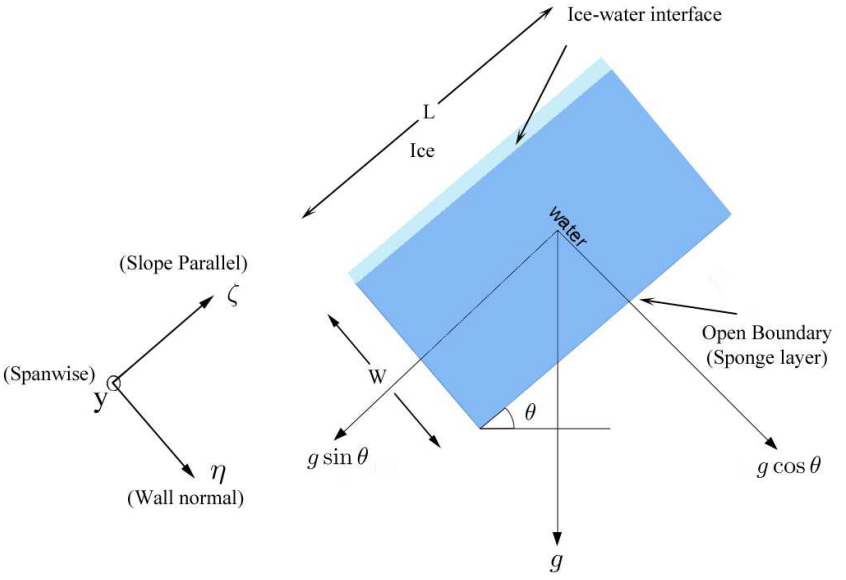

Figure 1: Schematic of the simulation domain. The ice face of length L is in contact with seawater beneath at initial temperature T_w and salinity S_w. At the bottom right, the domain has an open boundary condition using a sponge layer. Interface conditions at the ice (T_{int}; S_{int} and dissolution velocity V) are evaluated from heat and salt flux balances at that boundary.

(S_w) and density (ρ_w). The saline water has kinematic viscosity ν, thermal diffusivity κ_T and salinity diffusivity κ_S. As the flow involves only a small range of temperatures, the equation of state is closely approximated as linear without significant effects on the solution:

$$\rho^* = \rho_0(\beta S^* - \alpha T^*), \tag{2.7}$$

with coefficient of thermal expansion α and coefficient of haline contraction β. Domains of a given length having different slopes have different vertical heights due to the inclination. Thus we compare the flow and melt rate for different slopes at two given values of the global Grashof number (Gr, which is the relative strength of buoyancy to viscous force) and one value of the Stefan number (St),

$$Gr \equiv \frac{g\beta\Delta S L^3}{\nu^2}, \quad St \equiv \frac{\rho_s L_f}{\rho_w c_w (T_w - T_{int})}, \tag{2.8}$$

where, $[S_{int}, T_{int}]$ are the interface and $[S_w, T_w]$ are the far field salinity and temperature, $\Delta S = (S_w - S_{int})$ is the salinity anomaly, c_w is the specific heat, L_f is the latent heat of fusion for ice and ρ_s is the density of the ice The values of Gr and St are independent of slope because the simulations in section 4 show that the interface temperature and

salinity are independent of slope. The Prandtl number ($Pr = \nu/\kappa_T$) and Schmidt number ($Sc = \nu/\kappa_S$) are fixed.

Three relations are applied at the ice-water interface. The freezing point of saline water is closely approximated by a linear function of salinity and pressure.

$$T_{int} = a_s S_{int} + bP_{int} \simeq a_s S_{int}. \tag{2.9}$$

For the present study the effect on the freezing point of hydrostatic pressure difference within the limited domain size is negligible and the interface temperature is assumed to be solely dependent on interface salinity. The slope of the liquidus line is fixed at $a_s = -6 \times 10^{-2}$°C ‰$^{-1}$ (Holland & Jenkins 1999).

The second interface relation expresses the balance between latent heat flux Q_m^H of melting and the divergence of conductive heat fluxes at the interface,

$$Q_{ice}^H - Q_w^H = Q_m^H, \tag{2.10}$$

where Q_{ice}^H and Q_w^H are the heat fluxes to the interface in the ice and water, respectively.

The conductive transfer of heat into the ice has a negligible effect for ice temperatures within several degrees of the interface temperature (Kerr & McConnochie 2015). Although the typical ice core temperature is between -10°C to -30°C (Mellor 1960), in the present simulation we made finite ice approximation and neglected the diffusive heat flux into the ice ($Q_{ice}^H \sim 0$). If it is also assumed that the diffusion of heat at the interface is much faster than the advection of heat by the ablation velocity (i.e. $\kappa_T \partial^2 T/\partial\eta^2 >> V\partial T/\partial\eta\big|_{\eta=0}$, as $V << \kappa_T/\delta_T$, where δ_T is the diffusive thermal boundary layer thickness), (2.10) can be written as

$$\rho_w c_w \kappa_T \frac{\partial T}{\partial \eta}\bigg|_{\eta=0} = \rho_s V L_f, \tag{2.11}$$

where V is the ablation velocity. Positive ablation velocity indicates melting and retreat of the interface in the negative η-direction (at speed V) relative to the ice mass, or translation of the ice mass in the positive η-direction relative to the interface reference frame used here.

An analogous equation is used to describe the salt flux balance at the interface due to fresh water release and salt flux divergence

$$Q_{ice}^S - Q_w^S = Q_m^S. \tag{2.12}$$

Here Q_{ice}^S and Q_w^S are the diffusive salt fluxes to the interface in the ice and water, respectively, and Q_m^S is the fresh water flux associated with melting. The later can be expressed as $Q_m^S = \rho_s V(S_{ice} - S_{int})$. If the diffusive salt flux in ice is neglected then (2.12) can be written as

$$\rho_w \kappa_S \frac{\partial S}{\partial \eta}\bigg|_{\eta=0} = \rho_s V(S_{int} - S_{ice}). \tag{2.13}$$

In the present study the ice is considered fresh ($S_{ice} \simeq 0$). Hence the advective flux of salt from the ice (VS_{ice}) on melting is neglected. We impose wall-normal velocity $u_\eta = \rho_S V/\rho_w$ (Wells & Worster 2011) at the ice face side of the fluid domain. For cases giving V dependent on ζ we neglect effects of the mean gradient $du_\eta/d\zeta|_{\eta=0}$, as justified by Carey & Gebhart (1982).We neglect the effects of spatial and temporal variations of $u_\zeta|_{\eta=0}$ associated with the flow fluctuations and verified that the DNS solutions are unchanged if $u_\eta|_{\eta=0}$ is set to zero. The open ocean side of the computational domain is maintained as an open boundary by relaxing temperature and salinity back to its background temperature

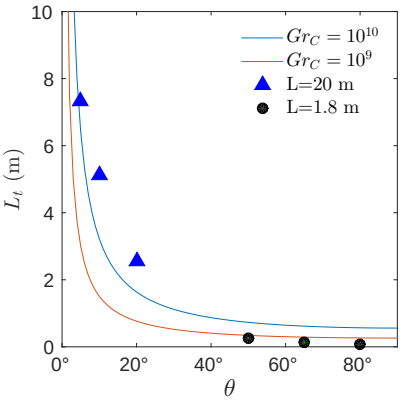

Figure 2: Simulated and theoretically predicted (2.14) laminar to turbulent transition length, where the prediction (curves) are based on the critical Grashof number for a vertical wall ($Gr_c^{\perp} = 10^9 - 10^{10}$). The simulated transition length L_t is calculated based on turbulent statistics from the simulations for $L = 1.8$ m and 20 m, respectively.

T_w and salinity S_w, respectively, through a 'sponge' region (Gayen & Sarkar 2011) at $0.5W \leqslant \eta \leqslant W$. The along-slope, span-wise velocities and scalar fields are relaxed towards the background state in the sponge region by adding damping functions $-\sigma(\eta)u_i(\eta, y, \zeta, t)$ (where $i = 2, 3$), $-\sigma(\eta)T^*(\eta, y, \zeta, t)$ and $-\sigma(\eta)S^*(\eta, y, \zeta, t)$ to the right-hand side of the momentum and scalar equations respectively where $\sigma(\eta)$ changes from 0 at $\eta = 0.5W$ to $1/\Delta t$ s^{-1} at $\eta = W$ based on the time step Δt. At the lower and upper boundaries of the domain, no-slip conditions are imposed for velocities and no-flux conditions are maintained for the temperature and salinity. Both T_{int} and S_{int} vary over the interface due to variation in the local heat and solute transport at the interface.

The solution is obtained using a mixed spectral/finite difference algorithm (Gayen *et al.* 2016). The wall-normal and slope-parallel spatial derivatives (η and ζ) are computed with second-order finite difference. The spanwise (y) direction is considered periodic and derivatives in this direction are treated with a pseudo-spectral method. Time-stepping is accomplished with a mixed implicit/explicit strategy with all terms involving viscous contribution being stepped with the Alternating Direction Implicit (ADI) method. All the other terms are treated with a low storage 3rd order Runge-Kutta method (Gayen 2012).

The physical dimension of the rectangular domain for the first set of simulations is $W = 0.4$ m, $D = 0.05$ m and $L = 1.8$ m. Additional simulations with a width doubled to $D = 0.1$ m, and the same W and L, show similar boundary layer properties and melt rates. A width of $D = 0.05$ m is used for the remainder of the simulations for the sake of computational efficiency. A second set of solutions are used $W = 4$ m, $D = 0.05$ m and $L = 20$ m. The corresponding grids have $256 \times 64 \times 1150$ and $256 \times 64 \times 1920$ points in the η, y and ζ direction, respectively. In order to resolve the salinity boundary layer and turbulent microscales for salinity, grid stretching is used in the η direction. All solutions rigorously satisfy grid resolution and grid convergence criteria as proposed in Gayen *et al.* (2014, 2016). Variable time stepping with a fixed Courant-Friedrichs-Lewy (CFL) number of $N_{CFL} = 0.5$ is used. The time step is calculated to be $\Delta t = (1/N_{CFL})[\Delta\eta/u_\eta, \Delta y/v, \Delta\zeta/u_\zeta]_{min}$ and varies significantly, from $O(10^{-3})$ s in the

turbulent regime to $O(10^{-2})$ s in the laminar regime. The fractional step method is used to evaluate dynamic pressure at each time step (Gayen & Sarkar 2011).

The slope angle θ is varied from 2° to 90°. In order to focus on the effect of slope on the melting process, the far-field temperature $T_w = 2.3°$ C and salinity $S_w = 35$ ‰ are fixed for all cases. All temperatures are measured with respect to the freezing point of pure water and therefore are quoted in Celsius. We fix $g = 10$ m s^{-2}, $\kappa_T = 1.285\times10^{-7}$ m^2 s^{-1}, $c_w = 3985$ J kg^{-1}K^{-1}, $\nu = 1.8\times10^{-6}$ m^2 s^{-1}, $\alpha = 6\times10^{-5}K^{-1}$ and $\beta = 8\times10^{-4}$ ‰$^{-1}$, taken from the physical properties of aqueous NaCl solutions at the far field condition (Washburn 1926; Weast *et al.* 1989). We use $\kappa_S = 7.2\times10^{-10}$ m^2 s^{-1} at 0° C (Josberger & Martin 1981) with a resultant $Sc = 2500$ at grid points adjacent to the interface. In the interior we use $\kappa_S = 3.6\times10^{-9}$ m^2 s^{-1} ($Sc = 500$, Gayen *et al.* 2016) in order to make the turbulence simulations feasible. The Prandtl number $Pr = 15$ is fixed throughout the domain. The primary numerical experiments are conducted using different slope angles at $Gr = 7.5\times10^{11}$ (for a domain length of 1.8 m) and $Gr = 10.28\times10^{14}$ (for domain length of 20 m).

The critical Grashof number for transitions from laminar to turbulent flow on a vertical wall varies from $Gr_c^{\perp} \sim 10^9 - 10^{10}$(Holman 2010; Josberger & Martin 1981; Turner 1979). A first approximation for the critical along-slope distance L_c beyond which the boundary layer becomes turbulent, based on the critical vertical height $L_c^{\perp}$, is

$$L_c \approx \frac{L_c^{\perp}}{\sin\theta} = \frac{1}{\sin\theta}\left(\frac{\nu^2 Gr_c^{\perp}}{g\beta\Delta S}\right)^{1/3}, \tag{2.14}$$

giving a critical Grashof number for the sloping interface as

$$Gr_c \approx \frac{Gr_c^{\perp}}{(\sin\theta)^3}. \tag{2.15}$$

Based on this assumption we calculated the transition length for various slope angles bounding the previously established critical $Gr_c^{\perp}$ (figure 2) and plotted the laminar to turbulent transition length (L_c) given by the DNS, where L_c is defined as the height where spanwise fluctuations (v_{rms}) reach 10% or more of the average up-slope flow. The results show that along-slope length to achieve turbulence increases rapidly with decreasing slope angles. Hence in order to simulate turbulent conditions at slopes $\theta \leqslant 20°$ we require the longer domain of 20 m.

3. Scaling Analysis

In contact with saline water warmer than the melting temperature, ablation of the ice face takes place and the resulting freshening of the water adjacent to the ice gives rise to a buoyant boundary layer plume. The plume can be divided into multiple layers (figure 3) having different force balances in the momentum budget and different balances of transport terms in the salinity equation. Within an inner layer against the ice face of thickness δ_i, buoyancy and either viscous (laminar flow field) or Reynolds stress (turbulent flow field) are the dominant terms in the momentum equation. Over this inner layer molecular diffusion of solute is an important, if not dominant, term in the salt budget. Similarly, thermal diffusion is important within a thickness δ_T. Outside the inner solutal boundary layer we define an outer layer, of thickness δ_0, in which the flow is inertial and buoyancy forces make a negligible contribution. Thus the thermal diffusive boundary layer may overlap the outer inertial boundary layer.

When the flow is laminar the whole inner buoyancy driven layer is dominated by viscosity and molecular diffusion (Wells & Worster 2011). When the plume is turbulent

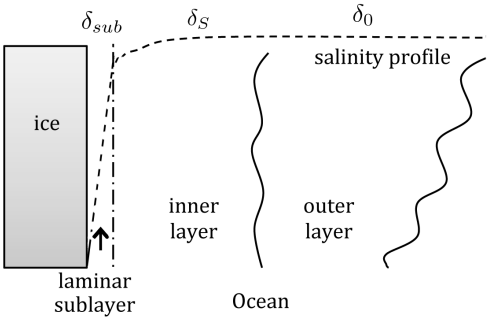

Figure 3: Schematic of different sections of the turbulent boundary layer based on the salinity profile in the wall normal direction (not to scale).

at large Grashof numbers, small-scale eddies add significantly to the momentum and solutal transport in much of the the inner buoyant layer, leaving a much thinner laminar sublayer (δ_{sub}) against the ice face in which eddy transport and turbulent kinetic energy production are negligible. The thickness of the δ_{sub} in the DNS solutions is found to be O(10) times smaller than the thickness δ_S of the inner salinity layer. The outer layer of the turbulent plume is dominated by Reynolds stress and turbulent transport of solute, leaving negligible molecular transport and the solute is relatively well mixed. Ambient water is brought into the outer layer through entrainment processes. These definitions for the various layers are consistent with a conceptual model previously proposed for natural thermal convection at a heated vertical boundary (Wells & Worster 2008). The thickness of the inner boundary layer and fluxes to and from the ice face can be estimated by examining the momentum and advection-diffusion equations (2.2-2.6). We predict different scaling laws for the laminar and turbulent cases.

3.1. *Laminar Boundary layer flows: viscous-buoyancy balance*

The laminar melt boundary scaling of Wells & Worster (2011) is briefly reviewed here in the context of a sloping ice face. In the inner layer δ_S and $\mathcal{L}$ are the characteristics length scales for the wall normal and the along slope directions, respectively, whereas δ_0 and $\mathcal{L}$ are characteristics length scales associated to the outer layer. At small Grashof numbers ($Gr < Gr_c$) or shallower slopes and quiescent far-field, the inertia terms inside the diffusive boundary layer are negligible, leaving a balance between viscous drag and buoyancy in the upslope flow (see the momentum equations (2.2-2.4)). The buoyancy is predominantly supplied by the salinity anomaly (ΔS) across the diffusive boundary layer:

$$\nu \frac{\partial^2 U_\zeta}{\partial \eta^2} \sim \nu \frac{U_\zeta}{\delta_S^2} \sim g \sin\theta \ \beta \Delta S. \tag{3.1}$$

The wall-normal derivatives in the boundary layer are the dominant contributions ($\partial/\partial\eta \gg \partial/\partial\zeta$ as $\delta_S \ll \mathcal{L}$) to both the viscous drag ($\nu\partial^2 U_\zeta/\partial\eta^2$) and the diffusion of solute. Outside the solutal diffusive boundary layer the buoyancy force is neglected and hence the inertia in the outer layer may balance the residual viscous drag force

generated by the up slope flow (Nilson 1985). This leads to

$$\frac{U_\zeta^2}{\mathcal{L}} \sim \nu \frac{U_\zeta}{\delta_0^2} \tag{3.2}$$

The convective salt transport by mean flow in (2.6) balances solute diffusion through the inner boundary layer:

$$U_\zeta \frac{\Delta S}{\mathcal{L}} \sim U_\eta \frac{\Delta S}{\delta_S} \sim \kappa_S \frac{\Delta S}{\delta_S^2}. \tag{3.3}$$

Here total velocity $u_i = U_i + u_i'$ is decomposed into the mean boundary layer flow U_i and fluctuating velocity component u_i' with the latter assumed to play a negligible role for laminar flow. We also assume that the salinity anomaly in the along-slope direction is equivalent to the salinity difference across the boundary layer. Combining (3.1) and (3.3) leads to the scaling of the thickness of the solutal boundary layer as

$$\delta_S \sim \delta_{S0} (\sin\theta)^{-\frac{1}{4}}, \tag{3.4}$$

where, δ_{S0} is the salinity boundary layer thickness for the case of a vertical ice face:

$$\delta_S \sim \left(\frac{\nu \kappa_S \mathcal{L}}{g \beta \Delta S} \right)^{\frac{1}{4}}, \tag{3.5}$$

or equivalently

$$\frac{\delta_S}{\mathcal{L}} \sim Gr_{\mathcal{L}}^{-1/4} Sc^{-1/4}, \tag{3.6}$$

with the local Grashof number ($Gr_{\mathcal{L}} = g\beta\Delta S \mathcal{L}^3/\nu^2$), based on the up-slope distance $\mathcal{L}$. From (2.13) the ablation rate can be estimated as $V \sim (\rho_w \kappa_S \Delta S)/(\rho_S S_{int} \delta_S)$, which gives

$$V \sim V_0 (\sin\theta)^{1/4}. \tag{3.7}$$

Here the ablation rate for vertical ice face is

$$V_0 \sim \frac{\rho_w \Delta S}{\rho_S S_{int}} \left(\frac{g \beta \Delta S \kappa_S^3}{\nu} \right)^{1/4} \mathcal{L}^{-1/4}, \tag{3.8}$$

or

$$\frac{V_0 \mathcal{L}}{\kappa_S} \sim \left(\frac{\rho_w \Delta S}{\rho_S S_{int}} \right) Gr_{\mathcal{L}}^{1/4}. \tag{3.9}$$

This predicts that the ablation rates decrease in the along slope direction as $\zeta^{-1/4}$ and with slope angle as $(\sin\theta)^{1/4}$. This scaling is consistent with the theory of laminar dissolution of a vertical ice face ($\theta = \pi/2$) found by Wells & Worster (2011). Considering the diffusive heat transport in the thermal boundary layer, the ablation rate from (2.11) must satisfy

$$V \sim -\frac{\rho_w c_w \kappa_T \Delta T}{\rho_S L_f \delta_T}. \tag{3.10}$$

Equating (3.10) and (3.7), the thermal boundary layer thickness δ_T can then be expressed as

$$\delta_T \sim \delta_{T0} (\sin\theta)^{-\frac{1}{4}}, \tag{3.11}$$

where, the thermal boundary layer thickness δ_{T0} for the case of a vertical ice face is

$$\delta_{T0} \sim \frac{c_w \kappa_T S_{int}}{\kappa_S L_f} \frac{\Delta T}{\Delta S} \left(\frac{\nu \kappa_S \mathcal{L}}{g \beta \Delta S} \right)^{\frac{1}{4}}, \tag{3.12}$$

or in dimensionless form

$$\frac{\delta_{T0}}{\mathcal{L}} \sim \left(\frac{\rho_S}{\rho_w} \frac{S_{int}}{\Delta S} \right) StLeGr_{\mathcal{L}}^{-1/4} Sc^{-1/4}, \tag{3.13}$$

Here $Le = \kappa_T/\kappa_S$ is the Lewis number. The thermal boundary layer thickness also shows a similar dependence on the up-slope distance and slope angle as that for the solutal boundary layer (3.5, 3.6). Scaling of the outer layer is (using 3.2 and 3.5)

$$\frac{\delta_0}{\mathcal{L}} \sim Sc^{1/2} \frac{\delta_S}{\mathcal{L}} \sim Gr_{\mathcal{L}}^{-1/4} Sc^{1/4}, \tag{3.14}$$

which is similar to the inner solutal boundary layer thickness and increases with length.

3.2. *Turbulent boundary layer flows: boundary layer inertia-buoyancy balance*

At large Gr, the boundary layer becomes unstable to both buoyancy and shear driven instabilities leading to small scale motions (Holman 2010; Josberger & Martin 1981; Gayen *et al.* 2016). Away from the ice face in the outer layer, diffusive transport is negligible and there is a balance in (2.6) between advection of solute by the mean flow and turbulent solute transport, leading to

$$\frac{U_\zeta \Delta S}{\mathcal{L}} \sim \frac{\overline{u'S'}}{\delta_0}. \tag{3.15}$$

There is potentially a regime, at intermediate Gr, in which turbulent transport of solute dominates over molecular transport while viscous stress remains important relative to Reynolds stress. However, here we consider a regime, at very large Gr, in which Reynolds stresses $\overline{u_i' u_j'}$ produced by the small scale motions dominate over the viscous stress and establish a dominant balance with local buoyancy in the inner layer. Thus we assume

$$\frac{\partial}{\partial \eta} \overline{u_\eta' u_\zeta'} \sim \frac{u_\eta'^2}{\delta_S} \sim g \sin\theta \ \beta \Delta S, \tag{3.16}$$

along with local isotropy ($u_\eta' \sim u_\zeta' \sim v'$).

For this turbulent case small scale fluctuations contribute to solute transport in the inner layer and the mean convective transport becomes relatively small, as indicated by the ratio of these terms $(\overline{u'S'}/\delta_S)/(U_\zeta \Delta S/\mathcal{L}) \sim \delta_0/\delta_S \gg 1$ (using 3.15). This is consistent with previous studies of natural convection at a heated vertical boundary (George & Capp 1979; Tsuji & Nagano 1988; Wells & Worster 2008). The solute transport by fluctuations balances, to leading order, the diffusive transport of salt giving

$$\frac{\partial \overline{u_\eta' S'}}{\partial \eta} + \frac{\partial \overline{u_\zeta' S'}}{\partial \zeta} \sim \kappa_S \frac{\partial^2 S}{\partial \eta^2} \rightarrow \frac{\overline{u_\eta' S'}}{\delta_S} \sim \kappa_S \frac{\Delta S}{\delta_S^2}, \tag{3.17}$$

where S' is the salinity fluctuation and $\partial/\partial\eta \gg \partial/\partial\zeta$. For a vertical ice face the fluctuations in the salinity field S' and density field ρ' scale with ΔS and $\Delta\rho$ and (3.16, 3.17) lead to turbulent boundary layer thickness and ablation rates:

$$\delta_{S0} \sim \left(\frac{\kappa_S^2}{g \beta \Delta S} \right)^{1/3} \text{and} \quad V_0 \sim \frac{\rho_w \Delta S}{\rho_s S_{int}} \left(g \beta \Delta S \kappa_S \right)^{1/3}. \tag{3.18}$$

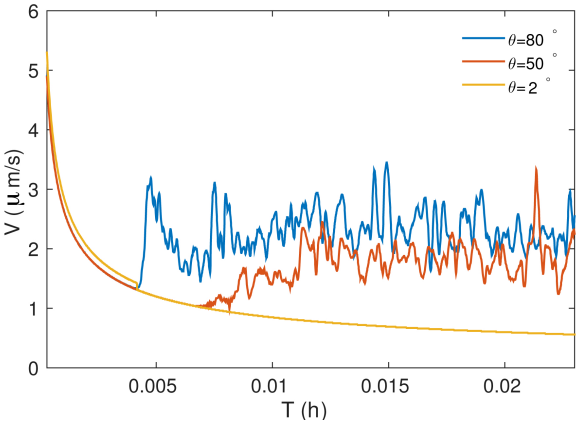

Figure 4: Temporal evolution of ablation rate ($\mu m/s$) measured at the mid length for slope angle $\theta, = 2°$, 50° and 80° in the 1.8 m domain.

Kerr & McConnochie (2015) reported scaling for the ablation velocity in this vertical case having this same dependence $V_0 \sim (g\beta\Delta S)^{1/3}$ but with $V_0 \sim (\kappa_S^2/\nu)^{1/3}$. The present theory neglects the effect of viscosity, which is assumed small compared with the Reynolds stress in the inner layer.

When the ice face is inclined, the fresh water flux due to ablation generates stratification, which inhibits the turbulent fluctuations. Hence, salinity fluctuations S' cannot directly scale with salinity anomaly ΔS across the boundary layer. Another independent equation is required to solve for S'. We assume that the mean density gradient in the inner stratified layer scales with $\Delta\rho/\delta_S$ and the frequency of turbulent fluctuations (the eddy turnover rate $1/\Delta t$) scales with the buoyancy frequency N. Hence $\Delta t \sim 1/N \sim [\rho_0\delta_S/g\Delta\rho]^{1/2}$, where $N^2 = -(g/\rho_0)d\rho/dz \sim (g/\rho_0)\Delta\rho/\delta_S$. This leads to a simple linearised equation for density fluctuation:

$$\frac{\partial\rho'}{\partial t} \sim u'_\eta \frac{\partial\overline{\rho}}{\partial\eta} \rightarrow \frac{\rho'}{\Delta t} \sim \frac{u'_\eta \Delta\rho}{\delta_S}. \tag{3.19}$$

These assumptions may not hold for near-vertical ice faces where the effect of local stratification becomes negligible. Substituting the timescale in (3.19), the density and salinity fluctuations ($S' \sim \rho'/\beta\rho_0$) become

$$\rho' \sim {u_\eta}' \sqrt{\frac{\Delta\rho\rho_0}{g\delta_S}}, S' \sim {u_\eta}' \sqrt{\frac{\Delta S}{g\beta\delta_S}}. \tag{3.20}$$

From (3.16), (3.17) and (3.20) salinity fluctuations scales as

$$S' \sim \Delta S(\sin\theta)^{1/2}, \tag{3.21}$$

and the solutal boundary layer thickness becomes

$$\delta_S \sim \delta_{S0}(\sin\theta)^{-2/3}, \tag{3.22}$$

where δ_{S0} is the solutal boundary layer thickness for the case of a vertical ice face and turbulent convection. In dimensionless form:

$$\frac{\delta_{S0}}{\mathcal{L}} \sim Gr_{\mathcal{L}}^{-1/3} Sc^{-2/3}. \tag{3.23}$$

Hence, δ_{S0} and δ_S are independent of up-slope distance. From (2.13) the ablation velocity becomes

$$V \sim V_0(\sin\theta)^{2/3}, \tag{3.24}$$

where the ablation velocity (3.18) for a vertical ice face is

$$\frac{V_0\mathcal{L}}{\kappa_S} \sim \left(\frac{\rho_w \Delta S}{\rho_S S_{int}}\right) Gr_{\mathcal{L}}^{1/3} Sc^{2/3}. \tag{3.25}$$

Thus ablation rates are predicted to be independent of distance along the slope and to increase with the slope angle as $(\sin\theta)^{2/3}$. Using (2.11) and (3.24) we solve for the thermal boundary layer thickness

$$\delta_T \sim \delta_{T0}(\sin\theta)^{-2/3}, \tag{3.26}$$

where for the vertical case

$$\delta_{T0} \sim \frac{c_w \kappa_T S_{int}}{\kappa_S L_f} \frac{\Delta T}{\Delta S} \left(\frac{\kappa_S^2}{g\beta\Delta S}\right)^{1/3}, \tag{3.27}$$

or

$$\frac{\delta_{T0}}{\mathcal{L}} \sim \left(\frac{\rho_S S_{int}}{\rho_w \Delta S}\right) St^{-1} LeGr_{\mathcal{L}}^{-1/3} Sc^{2/3}. \tag{3.28}$$

Like the inner solutal boundary layer, the inner thermal boundary layer has thickness independent of distance along the ice-interface.

The outer layer scaling can be established independently using entrainment characteristics. Continuity (2.1) for the mean flow in the outer layer shows

$$\frac{U_\zeta}{\mathcal{L}} \sim \frac{U_\eta}{\delta_0}. \tag{3.29}$$

The mean normal velocity U_η is equivalent to the entrainment velocity and is assumed to be linearly proportional to the along slope velocity, $U_\eta \sim EU_\zeta$, where E is the entrainment coefficient (Morton *et al.* 1956). This leads to

$$\delta_0 \sim E\mathcal{L}. \tag{3.30}$$

Similar scaling was suggested for the outer layer in the case of natural thermal convection at a heated vertical boundary (Wells & Worster 2011), for turbulent wall plumes driven by a uniformly distributed wall buoyancy flux (Cooper & Hunt 2010) and also for the melt boundary layer at a vertical ice wall (Kerr & McConnochie 2015; Gayen *et al.* 2016). Under an inclined ice face E is likely to be dependent on the slope angle, potentially following the result of Ellison & Turner (1959) for a dense plume flowing down a sloping boundary. For our case of melting of a sloping ice face, the result is an outer layer thickness that grows linearly with distance along the slope.

4. Results

All simulations were initiated with uniform temperature and salinity. White noise was imposed in the velocity field, concentrated near the interface. The initial ablation rate is large, as shown in figure 4, but it quickly slows down and reaches a statistically steady value. In the steady state for most of cases, high frequency variations are observed in the ablation rates and the interface temperatures (not shown here), as a result of turbulent fluctuations inside the boundary layer. The time to reach steady

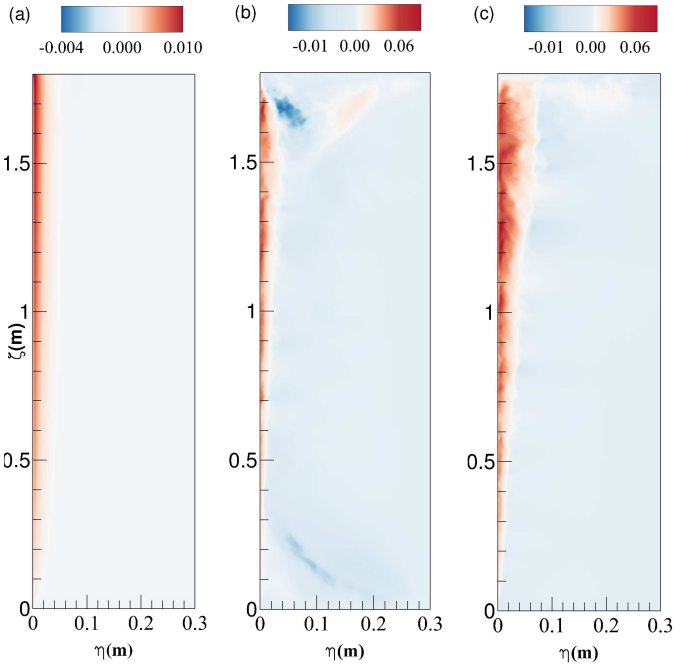

Figure 5: Snapshots of the along-slope velocity u_ζ (m/s) on a vertical $\zeta - \eta$ plane normal to the ice face for slope angles (a) $\theta = 2°$, (b) 50° and (c) 80°, respectively, with $L = 1.8$ m.

state decreased with increasing slope angle (figure 4). For the laminar boundary layer at $\theta = 2°$ temporal variability is absent and the simulation takes significantly longer to reach a steady state. The steady state ablation rate decreases for shallower angles.

Snapshots of the slope-parallel velocity for the 1.8 m and 20 m domains are shown in figures 5 and 6, respectively. Snapshots of the temperature and salinity field for a 1.8 m domain are shown in figure 7a and 7b, respectively. Buoyant water with low salinity is released from the interface and forms a very thin boundary layer (figure 7b) with upslope flow adjacent to the ice face. At the same time, a cooled outer boundary layer forms with downslope flow extending far beyond the inner salinity boundary layer (figure 7a). This bi-directional flow was previously predicted for a vertical ice face (Nilson 1985), was observed in laboratory experiments (Josberger & Martin 1981; Kerr & McConnochie 2015) and numerical simulations (Gayen *et al.* 2016). The inner boundary flow accelerates with upslope distance from the bottom of the domain and at the same time spreads outward due to laminar diffusion and turbulent entrainment of the quiescent ambient fluid. Flow structures inside the boundary layer are similar for turbulent cases at different slope angles.

For a given slope length, the buoyancy force in the along-slope direction decreases as the slope angle becomes shallower, resulting in weaker upslope flow. The wall-normal component of buoyancy keeps the upslope plume in contact with the wall and tends to separate it from the downslope flow (as shown in figure 5b). For the domain length of $L = 1.8$ m with slope angle $\theta \leqslant 30°$, the effective Grashof number is smaller than the the critical Grashof number ($Gr^\perp < Gr_c^\perp$) and the flow field is expected to be laminar. However, for the 20 m domain turbulence arises even for slopes as small as $\theta = 5°$ (figure 6a).

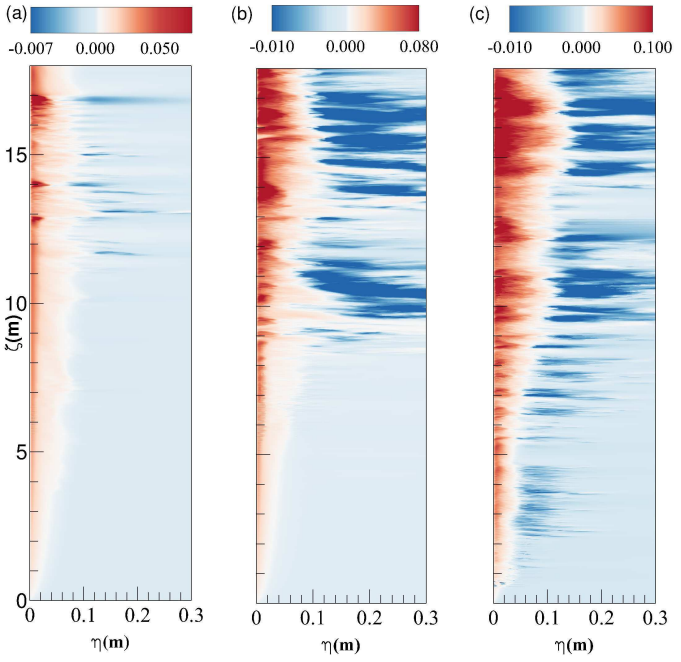

Figure 6: Similar to figure 5, along-slope velocity with θ = (a) 5°, (b) 10° and (c) 20°, respectively, for L = 20 m. The slope-normal distance η is enlarged by approximately 10 times relative to the slope-parallel scale in order to more clearly show the turbulent activity inside the boundary layer.

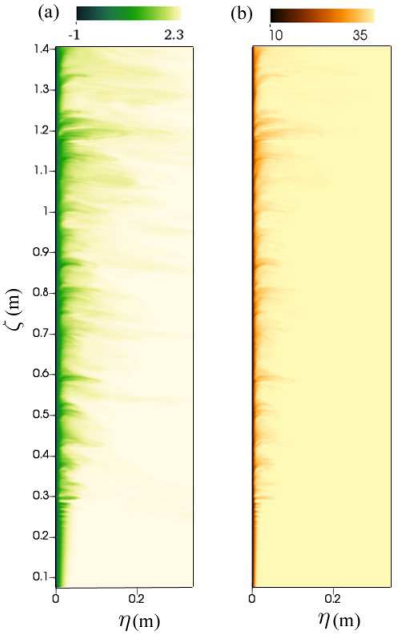

Figure 7: Snapshots of (a) temperature field T (°C) and (b) salinity field S (‰) for $\theta = 50°$.

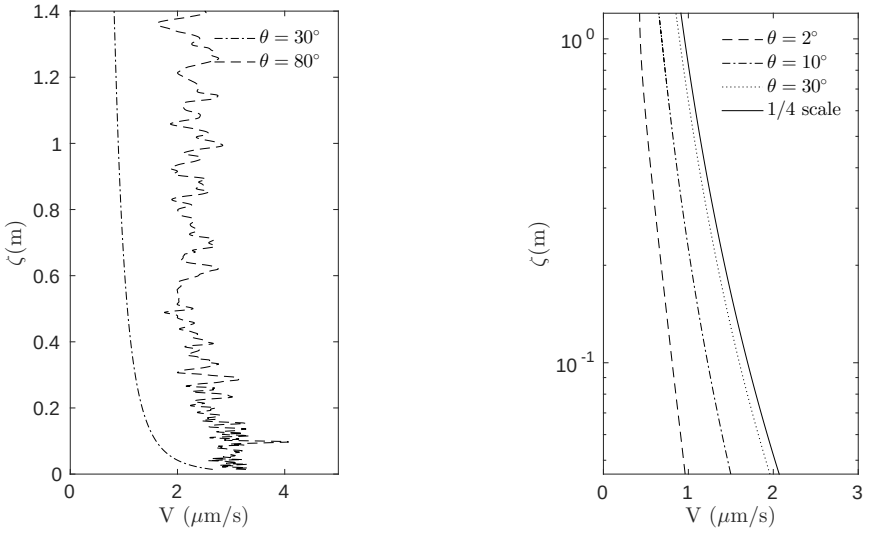

Figure 8: (a) Along-slope profiles of instantaneous laminar ($\theta = 30°$) and turbulent ($\theta = 80°$) dissolution rates. (b) Instantaneous laminar dissolution rates for $\theta = 2°$, $10°$ and $30°$, respectively, as a function of along-slope distance (in logarithmic scale) for $L = 1.8$ m, along with the theoretical 1/4 scaling (3.7) for laminar ablation rate for an arbitrary slope angle (continuous line). Values are taken after the flow field reaches quasi-steady state.

In figure 8a, the ablation rates are compared for laminar and turbulent cases (slopes $\theta = 30°$ and $\theta = 80°$) in the smaller domain. For $\theta = 80°$ a maximum ablation rate is observed around $\zeta = 0.05 - 0.075$ m from the bottom edge, where transition from laminar to turbulent flow takes place. Above this transitional region the turbulent ablation rate becomes statistically invariant with the along-slope distance. Similar observations were reported in laboratory experiments (Josberger & Martin 1981; Kerr & McConnochie 2015) and DNS of the vertical case (Gayen *et al.* 2016).

For $\theta = 30°$ and $L = 1.8$ m in figure 8a the entire boundary layer is laminar and the ablation rate decreases with along-slope distance. In order to estimate the power law relation of the ablation rate and along-slope distance, the ablation rates for $\theta = 2°, 10°$ and $30°$ are plotted over the slope length on a logarithmic scale (figure 8b). Consistent with the theoretical estimation in (3.7), the simulated laminar ablation rates decrease with up-slope distance from the base as $\zeta^{-1/4}$.

Time-averaged ablation rates at mid-length are shown in figure 9a, where the rates are averaged over 8-10 turnover times τ_b at statistically steady state. Here, $\tau_b = \left[L/g\beta\Delta S\right]^{1/2}$ is calculated based on the effective domain length L and characteristic velocity scale $[g\beta\Delta SL]^{1/2}$. Both laminar and turbulent ablation rates monotonically increase with the slope angle. The turbulent ablation rates are more sensitive to the ice face inclination than are the laminar rates. The laminar cases show a $(\sin\theta)^{1/4}$ dependence (3.7), whereas turbulent ablation rates follow a $(\sin\theta)^{2/3}$ dependence (figure 9b). Both of these behaviours are predicted by the theoretical scaling in (3.7) and (3.24). In figure 10a we plot the thermal (δ_T) boundary layer thickness as a function of slope

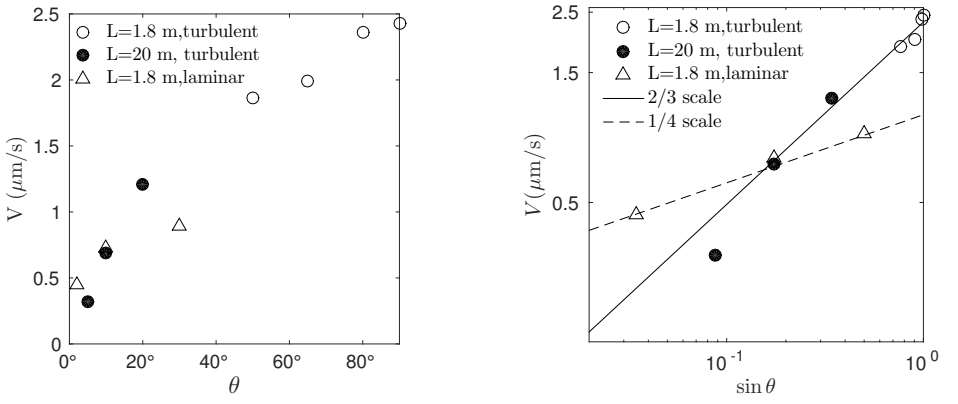

(a) (b)

Figure 9: Time averaged ablation rates at mid-length as functions of (a) slope angle θ and (b) $\sin\theta$. In (b) scales are logarithmic. Lines show the predicted 1/4 (dashed line) and 2/3 (solid line) power laws as predicted by (3.7) and (3.24). • turbulent boundary layer with $L = 1.8$ m; ∘ turbulent boundary layer with $L = 20$ m, △ laminar boundary layer with $L = 1.8$ m.

angle, where δ_T is measured as the e-folding distance from the ice-water interface. The measured boundary layer thickness increases with decreasing slope angle, with trends again depending on whether the boundary layer is laminar or turbulent. The thickness of the thermal boundary layer for laminar flow increases as $(\sin\theta)^{-1/4}$ (figure 10b). For turbulent flow the layer thickness is more sensitive to the slope angle and approximately follows $(\sin\theta)^{-2/3}$. Both behaviours are again consistent with the theoretical scaling in (3.11) and (3.26). The corresponding thickness of the salinity boundary layer (figure 11) behaves in an identical fashion and is approximately one half of the thermal boundary layer thickness.

The wall-normal advective buoyancy flux ($gu_\eta\rho^*/\rho_0$) based on wall-normal velocity u_η and density anomaly ρ^* is shown in figure 12a. Though the wall-normal buoyancy flux shows significant spatial variability associated with strong turbulent patches, the averaged value is negative. The magnitude of the averaged advective buoyancy flux shows increasing magnitude with the slope angle as $(\sin\theta)^{2/3}$ (see figure 12b). The ablation rate is also coupled to the net transport of buoyancy across the boundary layer. Therefore, the trend in buoyancy flux with slope angle is consistent with the change in ablation rate with slope angle as shown in (3.24). Under the conditions used here, the turbulent advection ($g\langle u_\eta{}'\rho'/\rho_0\rangle$) accounts for more than 80% of the total advective buoyancy flux in the wall-normal direction. The scaling (3.24) for transport can be compared with previous experiments for turbulent natural convection beneath a forward facing inclined heated plane (Vliet & Ross 1975), where constant heat flux was imposed over the whole plane. In that case, the heat transfer coefficient, Nu (the normalised heat transport), varies as the 1/4 power of the flux Grashof number, Gr^*_F. This is effectively the 1/3 power of the Grashof number based on the temperature difference ΔT and modified gravity $g^* = g(\sin\theta)^2$ ($Gr^* = g^*\alpha\Delta T L^3/\nu^2$, and the extra $\sin\theta$ dependence is due to stratification). The result therefore suggests the heat transfer coefficient follows $Nu \sim (\sin\theta)^{2/3}$, as is observed here.

The turbulent kinetic energy (K), as denoted by $K = (1/2)u_i'u_i'$ with index

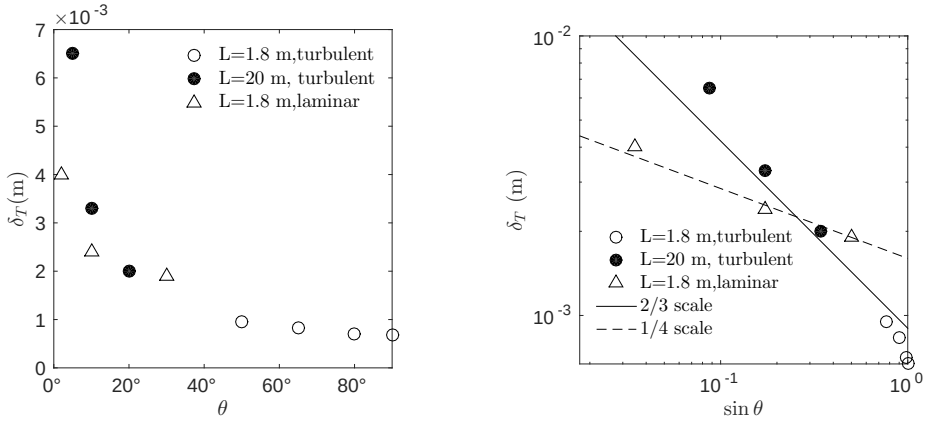

(a) (b)

Figure 10: Thermal boundary layer thickness δ_T (m) as a function of (a) slope angle θ and (b) $\sin\theta$ (scales are logarithmic). Solid and dotted line show the predicted scaling, (3.11) and (3.26), respectively. Symbols as in figure 9.

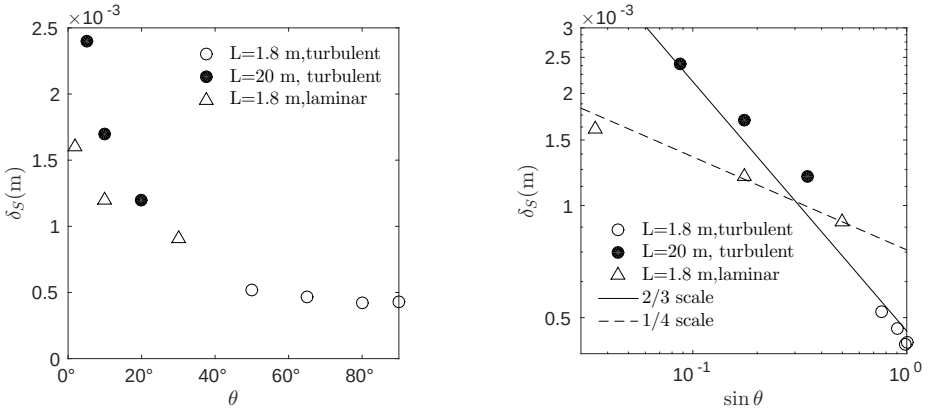

Figure 11: Salinity boundary layer thickness δ_S (m) as function of (a) slope angle θ and (b) $\sin\theta$ (scales are logarithmic). Solid and dotted line shows the predicted scaling of (3.4) and (3.22), respectively. Symbols as in figure 9.

representing η, y and ζ directions, is the energy associated with the fluctuating motions in the boundary layers. The fluctuating (primed) component $u_i' = u_i - U_i$, is calculated using spanwise spatial average U_i. The turbulent kinetic energy budget can be expressed as

$$\frac{\partial K}{\partial t} + u_j \frac{\partial K}{\partial x_j} = P - \varepsilon + B - \frac{\partial \Gamma}{\partial x_j}, \tag{4.1}$$

where P is the turbulent shear production

$$P = -\overline{u_i' u_j'} \frac{\partial U_i}{\partial x_j}, \tag{4.2}$$

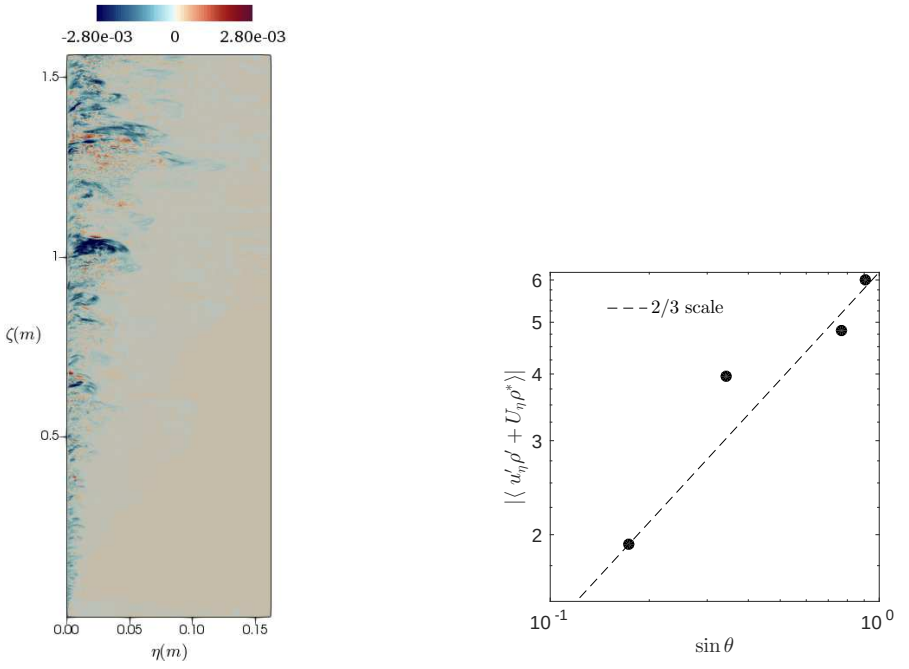

Figure 12: (a) Snapshot of wall-normal advective buoyancy flux (sum of mean ($U_\eta \rho^*$) and turbulent ($u'_\eta \rho'$) advective fluxes in kg s^{-1}/m^2), for $L = 1.8$ m and $\theta = 80°$, (b) Absolute value of time- and area-averaged total wall-normal buoyancy flux as a function of $\sin\theta$, where the real values are negative; scales are logarithmic. The dashed line has slope 2/3. The averaging is over a period $\tau \sim 10\tau_b$ and across the thickness of the boundary layer.

ε is the turbulent dissipation

$$\varepsilon = \nu \overline{\frac{\partial u'_i}{\partial x_j} \frac{\partial u'_i}{\partial x_j}}, \tag{4.3}$$

B is the turbulent buoyancy production

$$B = -g\overline{\rho' u'_\zeta} \sin\theta + g\overline{\rho' u'_\eta} \cos\theta, \tag{4.4}$$

and the term $\partial\Gamma/\partial x_j$ denotes the turbulent advection of K containing the pressure transport, turbulent transport and viscous transport, given as

$$\Gamma \equiv p' u'_i + \frac{1}{2}\overline{u'_i u'_i u'_j} - \nu \frac{\partial K}{\partial x_j}. \tag{4.5}$$

Snapshots of K for the shorter and longer domain are shown in figure 13a, 13b and 13c, 13d respectively. For all cases K increases in the upslope direction and the boundary layer thickens. For a given slope length, K is larger for the steeper ice faces. For the smaller slope, turbulence develops further along the ice interface (figure 13c and 13d).

The instantaneous turbulent production rate P, buoyancy production rate B, and viscous dissipation rate ε are shown in figure 14 for the steepest ($\theta = 90°$) ice face and in figure 15 for a small slope angle ($\theta = 10°$). Turbulent dissipation rate is always maximum at the ice face at all distances along the slope. A significant difference in the relative magnitude of turbulent production (compared with other terms in the

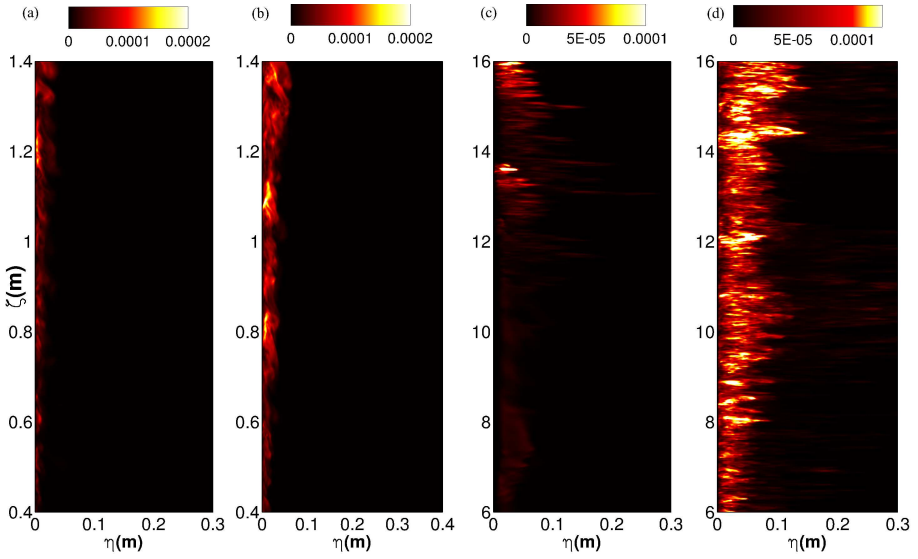

Figure 13: The instantaneous distribution of turbulent kinetic energy, K (m^2/s^3) in turbulent boundary layers for slope angle (a) $\theta = 50°$ and (b) $\theta = 90°$ for $L = 1.8$ m and (c) $\theta = 5°$ and (d) $\theta = 20°$ for $L = 20$ m. For (c) and (d) middle portion of the domain (actively turbulent region) is shown here and the slope perpendicular distance is enlarged by approximately 10 times relative to the slope-parallel scale in order to make the turbulent activity inside the boundary layer clearly visible.

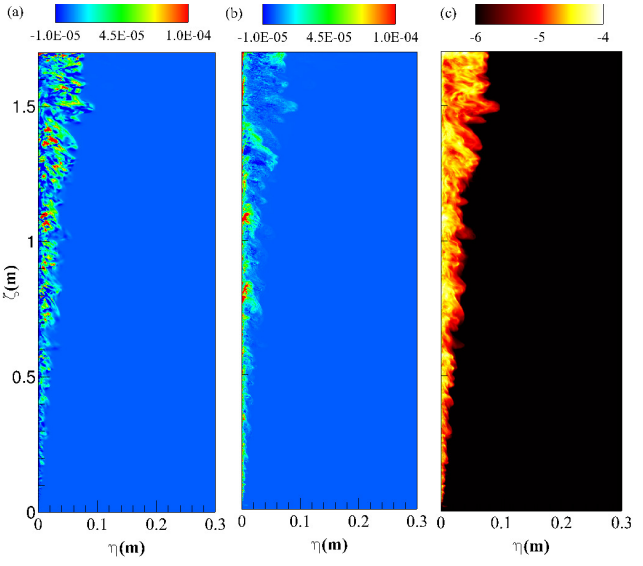

Figure 14: Snapshot of rates of (a) turbulent shear production, P (m^2/s^3), (b) buoyancy production B (m^2/s^3) and (c) viscous dissipation, ε (expressed in log scale) for $\theta = 90°$ in 1.8 m domain.

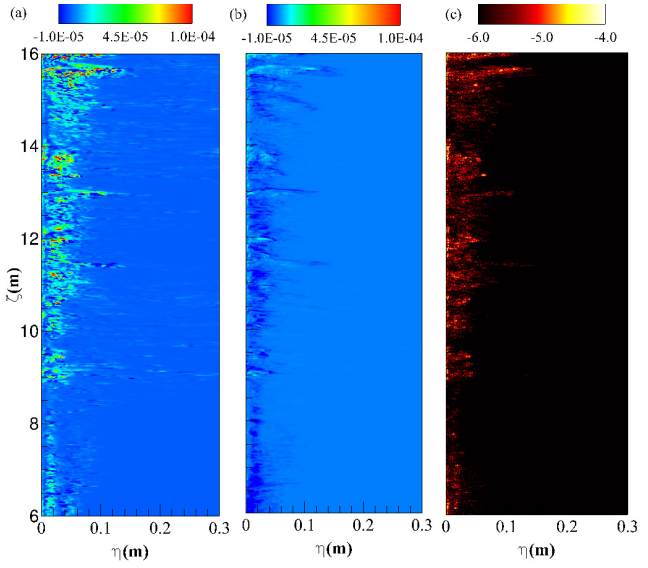

Figure 15: Snapshot of rates of (a) turbulent shear production, P ($\mathrm{m}^2/\mathrm{s}^3$), (b) buoyancy production B ($\mathrm{m}^2/\mathrm{s}^3$) and (c) viscous dissipation, ε (expressed in log scale) for $\theta = 10^\circ$ and $L = 20$ m. The slope-perpendicular distance is enlarged by approximately 10 times to the slope-parallel scale in order to clearly show the turbulent activity inside the boundary layer.

energy budget) is observed. For the shallower slopes, turbulent shear production is an order of magnitude greater than buoyancy production, whereas for a vertical ice face the magnitude of shear production is similar to that of buoyancy production. The relative contributions of turbulent fluxes towards the production of K are plotted in figure 16b, where the time and area averaged K, dissipation, shear and buoyancy production are denoted by, $\langle K\rangle, \langle\varepsilon\rangle, \langle T\rangle$ and $\langle B\rangle$ respectively, and are calculated as:

$$\langle K\rangle = \frac{1}{2\tau A}\int_A\int_\tau \overline{u_i' u_i'}\, dt\, dA, \tag{4.6}$$

$$\langle P\rangle = -\frac{1}{\tau A}\int_A\int_\tau \overline{u_i' u_j'}\frac{\partial U_i}{\partial x_j}\, dt\, dA, \tag{4.7}$$

$$\langle\varepsilon\rangle = \frac{1}{\tau A}\int_A\int_\tau \nu\overline{\frac{\partial u_i'}{\partial x_j}\frac{\partial u_i'}{\partial x_j}}\, dt\, dA \tag{4.8}$$

and

$$\langle B\rangle = \frac{1}{\tau A}\int_A\int_\tau g(-\overline{\rho' u_\zeta'}\sin\theta + \overline{\rho' u_\eta'}\cos\theta)\, dt\, dA. \tag{4.9}$$

The averaging time window is, $\tau \sim 10\tau_b$ and A is the area (in the ζ and η plane) containing the boundary layer in the upper-half of the domain length, where the boundary layer is fully turbulent. For steep inclination (figure 16a), K is large and the value of $\langle B\rangle$ is comparable or slightly larger than that of $\langle P\rangle$. For small slopes ($\theta \leqslant 20^\circ$) $\langle P\rangle$ dominates over $\langle B\rangle$.

The production of turbulence, either by velocity shear or buoyancy, is significantly influenced by density stratification and gravity at both limits of slope inclination.

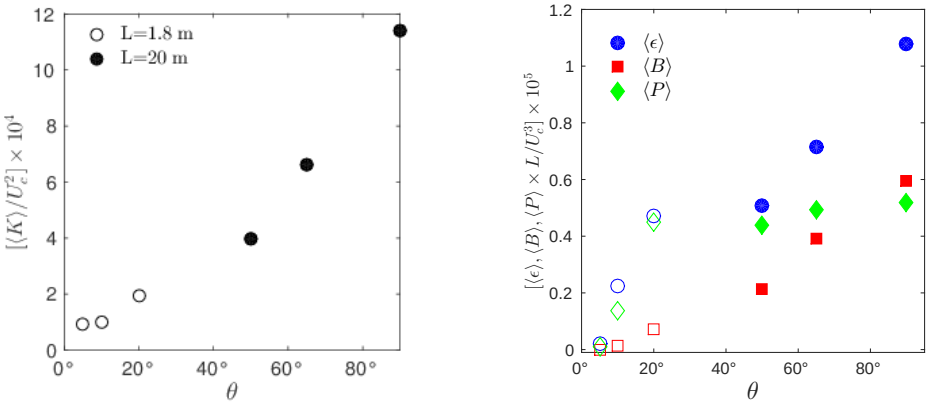

(a) (b)

Figure 16: Normalised time and area averaged turbulent statistics as function slope angle; (a) turbulent kinetic energy $\langle K\rangle$ is normalised by characteristic velocity scale $U_c \sim (g\beta\Delta SL)^{1/2}$, (b) turbulent dissipation $\langle\varepsilon\rangle$, buoyancy production $\langle B\rangle$, and turbulent shear production $\langle P\rangle$, for 1.8 m domain (filled symbols) and for 20 m domain (open symbols) normalised using the respective domain length L and velocity scale U_c.

When the ice face is steep ($\theta \geqslant 80°$), turbulent buoyancy flux (predominantly produced in the plume) is less impacted by the weak vertical (stable) buoyancy gradient produced by the solutal boundary layer. In contrast, the buoyancy production for small angles is reduced significantly by two mechanisms. First there is a large reduction in the buoyancy force in the along-slope direction ($g\sin\theta$) which produces the slope-parallel components of $\langle B\rangle$. In addition the development of stable stratification under the sloping ice face causes the turbulent advection in the wall-normal direction to decrease, resulting in smaller buoyancy production. For small slopes the velocity shear is large enough to produce turbulence and, as a result, the turbulent shear production becomes the dominant mechanism for maintaining turbulence in the boundary layer.

5. Discussion and Conclusions

This paper presents the first DNS of ice dissolution due to convection under a sloping ice face. We have simulated fully turbulent flow at geophysically relevant slopes ($\theta \leqslant 40°$) at temperature and salinities relevant to Antarctic conditions. The typical Grashof number based on the vertical height of the ice-seawater interface is of the order of $Gr^{\perp} \sim 10^{17} - 10^{19}$, for heights in the range 200 - 800 meters. Although this range is not achievable using DNS with present computational capacity, we have chosen large Grashof numbers ($Gr^{\perp} \sim 10^{10} - 10^{11}$), which are well above the critical $Gr_c^{\perp} \sim 10^9$ for the transition to turbulent convection on a vertical heated wall. The solutions confirm that these conditions ensure a steady turbulent mean flow. The boundary layer flow changes significantly with the slope. For steep angles a narrow upslope flow of relatively fresh buoyant water develops close to the wall. For small slope angles ($\theta < 20°$), the buoyant upslope flow is relatively weak due to the reduction of buoyancy force in the along-slope direction. However, the solutions at large Grashof numbers again show a turbulent flow.

Boundary layer properties and ablation rates are dependent on whether the

boundary layer is laminar or turbulent. Both the thermal and solutal boundary layer thicknesses increase with decreasing slope angles, resulting in the reduction of heat and salt transport to the interface and consequent reduction of the ablation rate. In the laminar case the ablation rate decreases with along-slope distance as $\zeta^{-1/4}$, consistent with theoretical scaling. In contrast the turbulent cases have ablation rates that are nearly uniform along the slope, as previously found for vertical ice faces (Kerr & McConnochie 2015; Gayen *et al.* 2016). We hypothesize that for domain lengths larger than those achieved in the present DNS, and having a Grashof number greater than the critical value, dissolution rate will be given by the asymptotic dynamics of turbulent boundary layer flow, and the present results can be extrapolated to geophysical scales following the scaling presented here. In that case, for a purely convective boundary layer, the ablation of ice faces into the ocean will follow $V \simeq (\sin\theta)^{2/3}$. This leads to a simple modification of the previously derived dependence of melt rate on the driving temperature difference (Kerr & McConnochie 2015; Gayen *et al.* 2016), now taking account of the interface slope as

$$V \simeq 8.98 \times (\Delta T_L)^{4/3}(\sin\theta)^{2/3} \quad \text{m/yr.} \tag{5.1}$$

An alternative scaling reported by Magorrian & Wells (2016) is based on a buoyant plume model and gives a greater sensitivity of melt rates on θ at shallow angles ($V \sim (\sin\theta)^{3/2}$) and an inverse dependence on slope angle ($V \sim 1/\sin\theta$) for near-vertical interfaces. Those trends are not reflected in the present DNS results. The discrepancy may result from a different regime of the convective boundary layer. The model of Jenkins (1991) and Magorrian & Wells (2016) assumes a regime in which the thickness of the inner laminar boundary layer near the ice face is controlled primarily by shear instability (Grossmann & Lohse 2000; Wells & Worster 2008) rather than convective instability as found here. The transition to this shear-dominated regime at steep slopes for saline convection was predicted to occur at $Gr \sim 10^{20}$, which occurs for vertical ice heights of hundreds of metres. The present study uses heights/domain lengths where the boundary layer on near-vertical interfaces remains controlled by turbulent convection. Hence it remains to be demonstrated that the transition can occur. Further discussion of transition between these two regimes can be found in McConnochie & Kerr (2017b).

The turbulent kinetic energy budget shows the presence of statistically steady turbulence in the simulated flow fields for slope angles as small as, $\theta = 5°$. For near vertical slopes ($\theta > 80°$) contributions to turbulent kinetic energy from shear production and buoyancy flux are comparable, with a slightly greater contribution from the buoyancy flux. For small slopes the production of turbulent kinetic energy by buoyancy fluxes is significantly smaller than the turbulent shear production. This potentially implies that the shear associated with large scale ambient geostrophic currents and barotropic tides in the ocean is more likely to contribute to the turbulent transport at the ice face and enhances the melt rate for small slopes.

The present study has focused on the effect of ice slope on melting that is driven by natural convection. The natural convection on its own can be viewed as a base, or reference case given that the natural convection will always be present irrespective of the magnitude and influence of shear associated with ambient geostrophic currents, internal waves or sub-glacial discharge plumes. The next step will be to include ambient stratification (McConnochie & Kerr 2016b), subglacial discharge of freshwater (McConnochie & Kerr 2017a) and ambient shear.

Acknowledgements

Computations were carried out using the Australian National Computational Infrastructure, through the National Computational Merit Allocation Scheme supported by the Australian Government. This work was supported by Australian Research Council grants DP120102772 and DP120102744. B.G. was supported by ARC DECRA Fellowship DE140100089 and an Australian Antarctic Division RJL Hawk Fellowship to BG.

REFERENCES

Beckmann, A. & Goosse, H. 2003 A parameterization of ice shelf-ocean interaction for climate models. *Ocean Modell.* **5** (2), 157–170.

Budd, W. F., Jacka, T. H. & Morgan, V. I. 1980 Antarctic iceberg melt rates derived from size distributions and movement rates. *Ann. Glaciol.* **1**, 103–112.

Carey, V. P. & Gebhart, B. 1982 Transport near a vertical ice surface melting in a saline water: experiments at low salinities. *J. Fluid Mech.* **117**, 403–423.

Cazenave, A. & Llovel, W. 2010 Contemporary Sea Level Rise. *Ann. Rev. Mar Sci.* **2** (1), 145–173.

Cooper, P. & Hunt, G. R. 2010 The ventilated filing box containing a vertically distributed source of buoyancy. *J. Fluid Mech.* **646**, 39–58.

Ellison, T. H. & Turner, J. S. 1959 Turbulent entrainment in stratified flows. *J. Fluid Mech.* **6**, 423–448.

Galton-Fenzi, B. K., Hunter, J. R., Coleman, R., Marsland, S. J. & Warner, R. C. 2012 Modeling the basal melting and marine ice accretion of the Amery Ice Shelf. *J. Geophys. Res.* **117**, C09031.

Gayen, B. 2012 Turbulence and internal waves in tidal flow over topography. PhD thesis, ProQuest Dissertations and Theses, Copyright - Database copyright ProQuest LLC; ProQuest does not claim copyright in the individual underlying works; Last updated - 2016-03-11.

Gayen, B., Griffiths, R. W. & Hughes, G. O. 2014 Stability transitions and turbulence in horizontal convection. *J. Fluid Mech.* **751**, 698–724.

Gayen, B., Griffiths, R. W. & Kerr, R. C. 2016 Simulation of convection at a vertical ice face dissolving into saline water. *J. Fluid Mech.* **798**, 284–298.

Gayen, B. & Sarkar, S. 2011 Direct and large eddy simulations of internal tide generation at a near critical slope. *J. Fluid Mech.* **681**, 48–79.

George, W. K. & Capp, S. P. 1979 A theory for natural convection turbulent boundary layers next to heated vertical surfaces. *Int. J. Heat Mass Transfer,* **22**, 813–826.

Gladish, C. V., Holland, D. M., Holland, P. R. & Price, S. F. 2012 Ice-shelf basal channels in a coupled ice/ocean model. *J. Glaciol.* **58**, 1227–1244.

Grossmann, S. & Lohse, D. 2000 Scaling in thermal convection: a unifying theory. *J. Fluid Mech.* **407**, 27–56.

Holland, D. M. & Jenkins, A. J. 1999 Modeling thermodynamic ice-ocean interactions at the base of an ice shelf. *J. Phys. Oceanogr.* **29**, 1787–1800.

Holman, J. P. 2010 *Heat Transfer (McGraw-Hill Series in Mechanical Engineering)*, 10th edn. Science Engineering & Math.

Huppert, H. E. & Turner, J. S. 1978 On melting icebergs. *Nature* **271**, 46–48.

Huppert, H. E. & Turner, J. S. 1980 Ice blocks melting into a salinity gradient. *J. Fluid Mech.* **100**, 367–384.

Jacobs, S. S., Jenkins, A., Giulivi, C. F. & Dutrieux, P. 2011 Stronger ocean circulation and increased melting under Pine Island Glacier ice shelf. *Narure Geosci.* **4**, 519–523.

Jenkins, A. 1991 A One-Dimensional Model of Ice Shelf-Ocean Interaction. *J. Geophys. Res.* **96** (C11), 20671–20677.

Jenkins, A. 2011 Convection-driven melting near the grounding lines of ice shelves and tidewater glaciers. *J. Phys. Oceanogr.* **41**, 2279–2294.

Jenkins, A., Dutrieux, P., Jacobs, S. S., McPhail, S. D., Perrett, J. R., Webb, A. T.

& White, D. 2010 Observations beneath Pine Island Glacier in West Antarctica and implications for its retreat. *Nature Geosci.* **3**, 468–472.

Josberger, E. G. & Martin, S. 1981 A laboratory and theoretical study of the boundary layer adjacent to a vertical melting ice wall in salt water. *J. Fluid Mech.* **111**, 439–473.

Kerr, R. C. 1994 Dissolving driven by vigorous compositional convection. *J. Fluid Mech.* **280**, 287–302.

Kerr, R. C. & McConnochie, C. D. 2015 Dissolution of a vertical solid surface by turbulent compositional convection. *J. Fluid Mech.* **765**, 211–228.

Lavergne, C., Palter, J. B., Galbraith, E. D., Bernardello, R. & Marinov, I. 2014 Cessation of deep convection in the open Southern Ocean under anthropogenic climate change. *Nat. Clim. Change* **4**, 278–282.

Magorrian, S. J. & Wells, A. J. 2016 Turbulent plumes from a glacier terminus melting in a stratified ocean. *J. Geophys. Res. Oceans* **121**, 4670–4696.

McConnochie, Craig D. & Kerr, Ross C. 2016b The effect of a salinity gradient on the dissolution of a vertical ice face. *J. Fluid Mech.* **791**, 589–607.

McConnochie, Craig D. & Kerr, Ross C. 2017a Enhanced ablation of a vertical ice wall due to an external freshwater plume. *J. Fluid Mech.* **810**, 429–447.

McConnochie, C. D. & Kerr, R. C. 2017b Testing a common ice-ocean parameterization with laboratory experiment. *J. Geophys. Res. Oceans* **122**, 5905–5915.

Mellor, M. 1960 Temperature gradient in the Antarctic ice sheet. *J. Glaciol.* **12**, 773–782.

Morgan, V. I. & Budd, W. F. 1978 The distribution, movements and melt rates of Antarctic Iceburghs. In *Iceberg Utilization: Proceedings of the First International Conference and Workshops on Iceberg Utilization for Fresh Water Production, Weather Modification and Other Applications Held at Iowa State University, Ames, Iowa, USA, October 2-6, 1977* (ed. A. A. Husseiny), pp. 220–228. Pergamon Press, New York.

Morrison, A. K., Hogg, A. M. & Ward, M. L. 2011 Sensitivity of the Southern Ocean overturning circulation to surface buoyancy forcing. *Geophys. Res. Lett.* **38**, L14602.

Morton, B. R., Taylor, G. & Turner, J. S. 1956 Turbulent Gravitational Convection from Maintained and Instantaneous Sources. *Proc. Royal Soc. A* **234**, 1–23.

Nilson, R. H. 1985 Countercurrent convection in a double-diffusive boundary layer. *J. Fluid Mech.* **160**, 181–210.

Paolo, F. S., Fricker, H. A. & Padman, L. 2016 Constructing improved decadal records of Antarctic ice shelf height change from multiple satellite radar altimeters. *Remote Sens. Environ.* **177**, 192–205.

Payne, A. J., Holland, P. R., Shepherd, A. P., Rutt, I. C., Jenkins, A. & Joughin, I. 2007 Numerical modeling of ocean-ice interaction under Pine Island Bay's ice shelf. *J. Geophys. Res.* **112**, C10019.

Piecuch, C. G & Ponte, R. M. 2014 Mechanisms of global-mean steric sea level change. *J. Clim.* **27** (2), 824–834.

Rignot, E. & Jacobs, S. S. 2002 Rapid bottom melting widespread near Antarctic ice sheet grounding lines. *Science* **296**, 2020–2023.

Rydt, J. D. & Gudmundsson, G. H 2016 Coupled ice shelf-ocean modeling and complex grounding line retreat from a seabed ridge. *J. Geophys. Res* **121**, 865–880.

Shepherd, A., Wingham, D. & Rignot, E. 2004 Warm ocean is eroding west antarctic ice sheet. *Geophys. Res. Lett.* **31** (23), n/a–n/a, l23402.

Slater, D. A., Goldberg, D. N., Nienow, P. W. & Cowton, T. R. 2016 Scalings for submarine melting at tidewater glaciers from buoyant plume theory. *J. Phys. Oceanogr.* **46** (6), 1839–1855.

Snow, K., Hogg, A. M., Sloyan, B. M. & Downes, S. M. 2016 Sensitivity of Antarctic Bottom Water to change in surface buoyancy fluxes. *J. Clim.* **29**, 313–330.

Spence, P., Griffies, S. M., England, M. H., Hogg, A. M., Saenko, O. A. & Jourdain, N. C. 2014 Rapid subsurface warming and circulation changes of Antarctic coastal waters by poleward shifting winds. *Geophys. Res. Lett.* **41**, 7089–7096.

Swingedouw, D., Fichefet, T., Huybrechts, P., Goosse, H., Driesschaert, E. & Loutre, M. F. 2008 Antarctic ice-sheet melting provides negative feedbacks on future climate warming. *Geophys. Res. Lett.* **35** (17), L17705.

Tsuji, T. & Nagano, Y. 1988 Turbulence measurements in a natural convection boundary layer along a vertical flat plate. *Int. J. Heat Mass Transfer* **31** (10), 2101 – 2111.

Turner, J. S. 1979 *Buoyancy effects in fluids*. Cambridge University Press.

Vliet, G. C. & Ross, D. C. 1975 Turbulent natural convection on upward and downward facing inclined constant heat flux surfaces. *J. Heat Transfer* **97** (4), 549–554.

Washburn, E. W. 1926 *International Critical Tables of Numerical Data, Physics, Chemistry and Technology*. Washington, DC: The National Academies Press.

Weast, Robert C, Astle, Melvin J, Beyer, William H & others 1989 *CRC handbook of chemistry and physics*, , vol. 1990. CRC press, Boca raton FL.

Wells, A. J. & Worster, M. G. 2008 A geophysical-scale model of vertical natural convection boundary layers. *J. Fluid Mech.* **609**, 111–137.

Wells, A. J. & Worster, M. G. 2011 Melting and dissolving of a vertical solid surface with laminar compositional convection. *J. Fluid Mech.* **687**, 118–140.

Woods, A. W. 1992 Melting and dissolving. *J. Fluid Mech.* **239**, 429–448.